



In Situ Monitoring of Structural and Valence Evolution during Electrochemical Desodiation/Sodiation Process of $\text{Na}_2\text{Fe}_{0.5}\text{Mn}_{0.5}\text{PO}_4\text{F}$

Yong Xie,^a Hongchun Wang,^a Rui Liu,^b Zhigang Wang,^a Wen Wen,^c Zheng Jiang,^c Zhengliang Gong,^{a,z} and Yong Yang^{a,b,*,z}

^aCollege of Energy, Xiamen University, Xiamen 361005, People's Republic of China

^bState Key Laboratory for Physical Chemistry of Solid Surface, Department of Chemistry, College of Chemistry and Chemical Engineering, Xiamen University, Xiamen 361005, People's Republic of China

^cShanghai Synchrotron Radiation Facility, Shanghai Institute of Applied Physics, Chinese Academy of Sciences, Shanghai 201204, People's Republic of China

$\text{Na}_2\text{Fe}_{0.5}\text{Mn}_{0.5}\text{PO}_4\text{F}$ as a cathode material for Na ion batteries is synthesized by a solid-state method. Synchrotron based in situ X-ray absorption near edge structure (XANES) and X-ray diffraction (XRD) techniques are used to study the electronic and crystal structure evolutions of $\text{Na}_2\text{Fe}_{0.5}\text{Mn}_{0.5}\text{PO}_4\text{F}$, complemented by electrochemical analyses during the electrochemical sodiation/desodiation. A reversible capacity of 107 mAh/g can be obtained at 12.4 mA/g with two well-defined voltage plateaus centered at 2.9 and 3.5 V vs. Na/Na^+ . Clear edge shifts in the Fe and Mn K-edge XANES are observed for $\text{Na}_2\text{Fe}_{0.5}\text{Mn}_{0.5}\text{PO}_4\text{F}$ at low current density (i.e., 8 mA/g), relating to the two plateaus in the charging curve associated with the $\text{Fe}^{2+}/\text{Fe}^{3+}$ and $\text{Mn}^{2+}/\text{Mn}^{3+}$ redox reactions sequentially. Increasing the charge current density to 100 mA/g, similar spectroscopic behavior is observed for Fe K-edge XANES. While, the Mn K-edge shift is smaller compared with this observed at 8 mA/g, indicating the sluggish reaction kinetic of $\text{Mn}^{3+}/\text{Mn}^{2+}$ redox couple. Continuous diffraction peaks shifts in in-situ XRD patterns of $\text{Na}_2\text{Fe}_{0.5}\text{Mn}_{0.5}\text{PO}_4\text{F}$ are observed throughout the charge-discharge process without emergence of new peaks, indicating of solid-solution processes. $\text{Na}_2\text{Fe}_{0.5}\text{Mn}_{0.5}\text{PO}_4\text{F}$ shows good structural reversibility during the electrochemical sodiation/desodiation.

© 2017 The Electrochemical Society. [DOI: 10.1149/2.0281714jes] All rights reserved.

Manuscript submitted September 5, 2017; revised manuscript received October 23, 2017. Published November 11, 2017.

Sodium-ion batteries have attracted significant attention as an alternative to lithium-ion batteries particularly in large-scale electric energy storage, due to the abundant sodium resources and its consequent cost advantages.¹⁻⁵ Sodium fluorophosphates-based compounds have attracted much attention as potential cathode materials for sodium-ion battery due to their relatively high voltage and good structural stability. Amongst the possible fluorophosphates materials, sodium iron and/or manganese fluorophosphates have been studied and tested extensively.⁶⁻¹⁰

In 2007, Ellis et al. first reported the sodium-based fluorophosphate ($\text{Na}_2\text{FePO}_4\text{F}$) as a novel cathode material for Li ion batteries.¹¹ $\text{Na}_2\text{FePO}_4\text{F}$ has a two-dimensional (2D) layered structure, leading to its electronic conductivity higher than that of LiFePO_4 . Since then, $\text{Na}_2\text{MPO}_4\text{F}$ ($M = \text{Fe}, \text{Mn}, \text{Co}, \text{etc.}$) materials have been extensively studied as cathode materials for both lithium and sodium ion batteries.¹² Recham et al. reported a sodium storage capacity of 120 mAh/g (about one electron exchange per formula unit) with an overall potential around 3 V for $\text{Na}_2\text{FePO}_4\text{F}$ prepared by the ionothermal approach.¹³ In the case of Co-based and Ni-based $\text{Na}_2\text{MPO}_4\text{F}$, both $\text{Na}_2\text{CoPO}_4\text{F}$ and $\text{Na}_2\text{NiPO}_4\text{F}$ crystallize in the space group $Pbcn$, which is identical to that of $\text{Na}_2\text{FePO}_4\text{F}$.⁹ The studies on the electrochemical performance of these materials are scarce due to their high electrode potential (>4.5 V vs. Na/Na^+), which results in severe decomposition of the most commonly used electrolytes.^{14,15} Different from the 2D layered structure of $\text{Na}_2\text{FePO}_4\text{F}$, $\text{Na}_2\text{MnPO}_4\text{F}$ takes up a three-dimensional tunnel structure with space group of $P2_1/n$.⁹ $\text{Na}_2\text{MnPO}_4\text{F}$ appears to be more attractive as cathode material than $\text{Na}_2\text{FePO}_4\text{F}$ due to its higher operating voltage (~ 3.5 V vs. Na/Na^+), which can improve the energy density of batteries.^{6,16-18} However, analogous to their olivine phosphate counterparts, $\text{Na}_2\text{MnPO}_4\text{F}$ shows poorer electrochemical active compared with $\text{Na}_2\text{FePO}_4\text{F}$, due to its very low intrinsic electrical conductivity and the large lattice distortions induced by Jahn-Teller effect from the Mn^{3+} ions. Particle-size reduction and conductive carbon-coating are effective approaches to enhance the electrochemical activity of $\text{Na}_2\text{MnPO}_4\text{F}$. Via decreasing particle size and uniform carbon coating, Wu et al. first reported

the electrochemically active of $\text{Na}_2\text{MnPO}_4\text{F}$ prepared by the sol-gel method.¹⁹ An initial discharge capacity of 98 mAh/g was achieved in a hybrid Na/Li-cell at a current density of 10 mA/g at 60°C. The electrochemical performance was further improved via the preparation of $\text{Na}_2\text{MnPO}_4\text{F}/\text{C}$ nanocomposite by spray drying method.¹⁶ Electrode performance of $\text{Na}_2\text{MnPO}_4\text{F}$ is still insufficient for the battery application, although the electrochemical activity of $\text{Na}_2\text{MnPO}_4\text{F}$ has been improved significantly. Partial substitution of Mn with Fe to get $\text{Na}_2\text{Fe}_x\text{Mn}_{1-x}\text{PO}_4\text{F}$ is another effective approach to enhance the electrochemical activity of $\text{Na}_2\text{MnPO}_4\text{F}$. It was reported that the crystal structure of $\text{Na}_2\text{Fe}_x\text{Mn}_{1-x}\text{PO}_4\text{F}$ changes from a 3D tunnel structure to a 2D layered structure with Fe content increases to $x > 0.75$.¹³ Wu et al. first demonstrated that a distinct plateau at ~ 4 V vs. Li/Li^+ can be obviously observed for $\text{Na}_2\text{Fe}_{0.3}\text{Mn}_{0.7}\text{PO}_4\text{F}$ in a hybrid Na/Li-cell, which could be assigned to the $\text{Mn}^{2+}/\text{Mn}^{3+}$ redox couple.¹⁹ Kawabe et al. reported that a discharge capacity of 110 mAh/g can be obtained for a well-optimized $\text{Na}_2\text{Fe}_{0.5}\text{Mn}_{0.5}\text{PO}_4\text{F}$ sample in sodium ion battery at a rate of 1/20 C (6.2 mA/g).⁶ It demonstrated a redox couple centered at 3.5 V vs. Na/Na^+ , corresponding to the $\text{Mn}^{2+}/\text{Mn}^{3+}$ redox reaction.

Currently, the research works on sodium-based fluorophosphate ($\text{Na}_2\text{MPO}_4\text{F}$) mainly focus on how to improve the electrochemical performance.^{12,20,21} However, to date no detailed structural and charge compensation analysis has been undertaken as to the sodium extraction/insertion mechanism of these materials, in light of their superior electrochemical performance. Clear understanding on the electronic and crystal structure evolution of $\text{Na}_2\text{Fe}_x\text{Mn}_{1-x}\text{PO}_4\text{F}$ during electrochemical sodium extraction/insertion is quite important for the development of $\text{Na}_2\text{MPO}_4\text{F}$ -type cathodes with enhanced electrochemical performance. Also to design better compositions in this system, the correlation between charge composition and the redox reactions of $\text{Fe}^{2+}/\text{Fe}^{3+}$ and $\text{Mn}^{2+}/\text{Mn}^{3+}$ should be systematically revealed. In-situ synchrotron based XRD and XAFS techniques are powerful tools to study the electrode evolution.²²⁻²⁷ In-situ XRD provides insight into the crystal structure evolution and reaction mechanism of electrode materials during charge/discharge. The metal K-edge XANES is a useful tool in tracking the change of oxidation state of chemical species during cycling.

In this paper, we report the results regarding the electronic and crystal structure evolution of $\text{Na}_2\text{Fe}_{0.5}\text{Mn}_{0.5}\text{PO}_4\text{F}$ during cycling by

*Electrochemical Society Member.

^zE-mail: zlgong@xmu.edu.cn; yyang@xmu.edu.cn

using in-situ Fe and Mn K-edge XANES and XRD techniques, complemented by electrochemical analyses. The effects of charge current density on charge compensation of $\text{Fe}^{2+}/\text{Fe}^{3+}$ and $\text{Mn}^{2+}/\text{Mn}^{3+}$ are revealed by in-situ XANES. A single phase solid solution Na^+ extraction/insertion process is revealed by in-situ XRD. Also a decrease in crystallinity related to the increase in the number of Jahn-Teller active Mn^{3+} ions is observed during the 3.8 V charge plateau corresponding to $\text{Mn}^{2+}/\text{Mn}^{3+}$ redox couple.

Experimental

Synthesis and characterization of $\text{Na}_2\text{Fe}_{0.5}\text{Mn}_{0.5}\text{PO}_4\text{F}/\text{C}$.—Carbon-coated $\text{Na}_2\text{Fe}_{0.5}\text{Mn}_{0.5}\text{PO}_4\text{F}$ material was synthesized by a simple solid-state method with sucrose as carbon source.⁶ The stoichiometric amount of NaF , $\text{FeC}_2\text{O}_4 \cdot 2\text{H}_2\text{O}$, $(\text{CH}_3\text{COO})_2\text{Mn} \cdot 4\text{H}_2\text{O}$, $\text{NH}_4\text{H}_2\text{PO}_4$, Na_2CO_3 were used as raw materials, and 10 wt% sucrose was also used as the carbon source. The starting materials were thoroughly mixed using a ball-mill at a speed of 500 rpm for 10 h using acetone as a dispersant. After evaporated the solvent, the mixture was heat treated at 400°C for 2 h in an argon atmosphere. Thus obtained powder was further ground by using the ball-mill after mixing with 10 wt% of acetylene black and pressed into pellets, then sintered at 650°C for 10 h in an argon atmosphere.

The crystalline phase of $\text{Na}_2\text{Fe}_{0.5}\text{Mn}_{0.5}\text{PO}_4\text{F}$ was identified by using a Rigaku Ultima IV X-ray Diffractometer (Rigaku Corporation, Japan) equipped with Cu K α radiation operated at 40 kV and 30 mA with a scanning rate of 5° per min. Rietveld refinement was performed using the GSAS (General Structure Analysis System) program to obtain the crystal structure parameters. The carbon content of the $\text{Na}_2\text{Fe}_{0.5}\text{Mn}_{0.5}\text{PO}_4\text{F}/\text{C}$ composite was determined to be 15.2 wt% by Vario EL III elemental analyzer (Elementar Analysen System GmbH, Germany).

Measurement of electrochemical performances.—The CR2025 coin-type cells were used to evaluate the electrochemical performance of $\text{Na}_2\text{Fe}_{0.5}\text{Mn}_{0.5}\text{PO}_4\text{F}/\text{Na}$ using a non-aqueous electrolyte (1 M NaClO_4/PC with 2 vol% fluoroethylene carbonate (FEC) as an additive) with Na foil as the anode and a glass fiber filter as the separator. To obtain the cathode slurry, the $\text{Na}_2\text{Fe}_{0.5}\text{Mn}_{0.5}\text{PO}_4\text{F}/\text{C}$ powder was mixed with acetylene black and polyvinylidene fluoride (PVDF) binder in a weight ratio of 8:1:1, followed by a ballmilling at 500 rpm for 3 h with N-methyl-2-pyrrolidone (NMP) as the solvent. The as-prepared slurry was then coated on Al foil with a diameter of 1.6 cm and dried at 120°C for 2 h under vacuum. The active material loading was $1.5\text{--}2.0 \text{ mg} \cdot \text{cm}^{-2}$. Cells were assembled in an argon-filled glove box. Electrochemical measurements were conducted on a LAND CT-2001A (Wuhan, China) battery test system. Galvanostatic charge/discharge tests were carried out at different current rates (1 C corresponding to 124 mA/g) at 30°C between 2.0 and 4.5 V.

In situ XRD and XANES measurements.—A standard CR2025 coin cell with small holes (2 mm in diameter) sealed well with Kapton tape in each side was used to perform the in situ XRD and XANES measurements. In situ Fe and Mn K-edge XANES spectra were collected in transmission mode at beamline BL14W1 at the Shanghai Synchrotron Radiation Facility (SSRF) (Shanghai, China) using a Si (111) double-crystal monochromator. Reference spectrum of each element for the energy calibration was collected using Fe and Mn metal foils. In order to explore the effects of current density on the electronic structure changes of $\text{Na}_2\text{Fe}_{0.5}\text{Mn}_{0.5}\text{PO}_4\text{F}$ during charging, the in situ XANES were collected at two different current density, a low current density of 8 mA/g (corresponding to 0.06 C, which is close to the quasi-equilibrium state) and a high current density of 100 mA/g (corresponding to 0.8 C). Once the in situ cell had been charged to a certain state, charging was halted, and XANES measurements were immediately performed. The XANES data were analyzed using the Athena program of IFEFFIT for background removal, absorption edge energy (E_0) determination and spectrum normalization, etc.

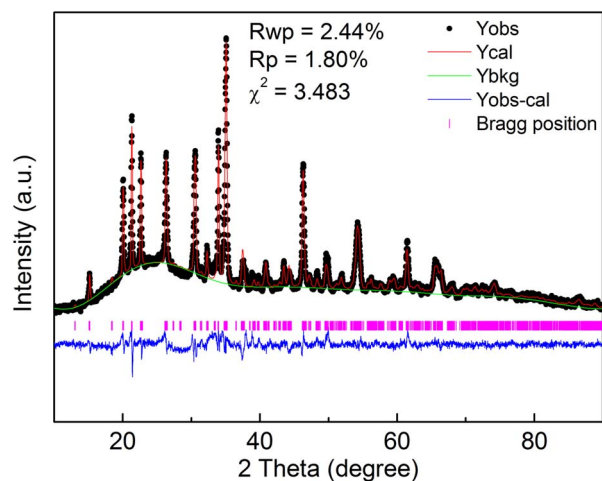


Figure 1. XRD pattern and Rietveld refinement of $\text{Na}_2\text{Fe}_{0.5}\text{Mn}_{0.5}\text{PO}_4\text{F}$ material. Yobs indicates observed pattern, Ycal indicates the calculated pattern, Ybkg indicates background, Yobs-cal indicates difference between observed pattern and calculated pattern, $R_{wp} = [\sum W_i |Y_i(\text{obs}) - Y_i(\text{cal})|^2 / \sum W_i Y_i^2(\text{obs})]^{1/2}$, $R_p = \sum |Y_i(\text{obs}) - Y_i(\text{cal})| / \sum Y_i(\text{obs})$, $R_{exp} = [(N_o - N_v) / \sum W_i |Y_i^2(\text{obs})|]^{1/2}$, $\chi = (R_{wp}/R_e)^2$.

In situ XRD patterns were collected at beamline BL14B1 of SSRF using a linear position sensitive silicon detector (MYTHEN 1K) with an exposure time of 60 s per step. The wavelength used was 0.6887 \AA . The current density used in the in situ XRD experiment was 24.8 mA/g .

Results and Discussion

Fig. 1 shows the XRD pattern of pristine $\text{Na}_2\text{Fe}_{0.5}\text{Mn}_{0.5}\text{PO}_4\text{F}$. All the diffraction peaks in pristine $\text{Na}_2\text{Fe}_{0.5}\text{Mn}_{0.5}\text{PO}_4\text{F}$ can be fully indexed in a monoclinic structure with space group $P2_1/n$, which is isostructural with $\text{Na}_2\text{MnPO}_4\text{F}$. No impurity phases were detected indicating the high phase purity and solid solution of $\text{Na}_2\text{FePO}_4\text{F}$ and $\text{Na}_2\text{MnPO}_4\text{F}$. The lattice parameters of $\text{Na}_2\text{Fe}_{0.5}\text{Mn}_{0.5}\text{PO}_4\text{F}$ from the results of the refinement are $a = 13.4776(6) \text{ \AA}$, $b = 5.2845(2) \text{ \AA}$, $c = 13.5374(8) \text{ \AA}$, $\beta = 119.669(4)^\circ$, $V = 837.76 \text{ \AA}^3$. Evidently, they are smaller than that of $\text{Na}_2\text{MnPO}_4\text{F}$ as expected from the smaller crystal radius of Fe^{2+} (0.75 \AA) compared to that of Mn^{2+} (0.81 \AA).^{9,17}

Fig. 2a shows typical charge-discharge profiles of $\text{Na}_2\text{Fe}_{0.5}\text{Mn}_{0.5}\text{PO}_4\text{F}$ cycled between 2.0 and 4.5 V at a current density of 12.4 mA/g . The initial discharge capacity is 107 mAh/g , corresponding to about 86% of theoretical capacity based on one sodium extraction/intercalation. Two well-defined voltage plateaus centered at 2.9 and 3.5 V can be observed. The cycling performance is shown in Fig. 2b. The data show good cycling stability with a capacity retention of 75% after 100 cycles. It also shows that the initial coulomb efficiency of $\text{Na}_2\text{Fe}_{0.5}\text{Mn}_{0.5}\text{PO}_4\text{F}$ electrode is relatively low (74.6%), then rapidly increase to about 90% in the first 10 cycles and gradually increase to around 98% in the subsequent cycles. The low coulomb efficiency can be attributed to side decomposition reactions of electrolyte when charging to a high voltage ($\sim 4.5 \text{ V vs. Na/Na}^+$).²⁸ Fig. 3 shows the first charge-discharge profiles and dQ/dV curves of $\text{Na}_2\text{Fe}_{0.5}\text{Mn}_{0.5}\text{PO}_4\text{F}$ cycled at various rates from 0.05 C to 4 C. A high discharge capacity of 112.8 mAh/g can be obtained at 0.05 C, which is similar to Kawabe et al.'s previous work (where a discharge capacity of 110 mAh/g at 0.05 C was obtained). The capacity decreases with increasing current rate. And the charge-discharge curves show serious polarization phenomena. The as prepared $\text{Na}_2\text{Fe}_{0.5}\text{Mn}_{0.5}\text{PO}_4\text{F}$ sample shows electrochemical performance similar to that of Kawabe et al.'s sample synthesized by the same method, both show similar voltage profiles and rate capability. The dQ/dV data evidenced two distinct redox couples centered at 2.9 and

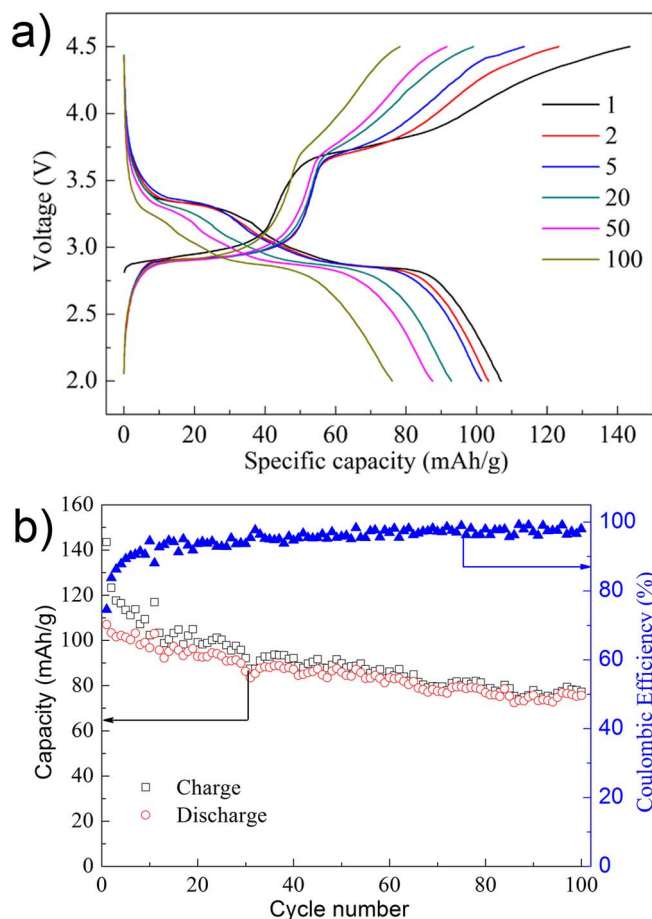


Figure 2. Charge/discharge profiles of Na₂Fe_{0.5}Mn_{0.5}PO₄F/Na cells over 2.0–4.5 V at a current density of 12.4 mA/g at 30°C (a), and the corresponding cyclic performance and coulombic efficiency (b).

3.5 V respectively. The polarization of the Mn²⁺/Mn³⁺ redox couple is obviously higher than that of Fe²⁺/Fe³⁺, which is similar to those observed in LiFePO₄ and LiMnPO₄.^{29,30} Compared with Mn²⁺/Mn³⁺ redox couple, Fe²⁺/Fe³⁺ redox couple shows better electrochemical reversibility. The intensity of Mn³⁺/Mn²⁺ redox peaks decrease rapidly with increasing current rate. With a 4 C rate, the Mn³⁺/Mn²⁺ redox couple becomes vague, only the Fe²⁺/Fe³⁺ redox couple is preserved and the capacity decreases to 47 mAh/g. Compared with Na₂FePO₄F, which shows two well-defined voltage plateaus centered at 3.0 and 2.9 V,^{13,15,21} Na₂Fe_{0.5}Mn_{0.5}PO₄F exhibits a higher discharge plateau at 3.5 V. A sloping discharge profile without obvious plateau was reported for Na₂MnPO₄F, the electrochemical performance is still unsatisfied with low discharge capacity and poor rate capability even after optimization.^{16,18} The high voltage plateau and good electrochemical performance of Na₂Fe_{0.5}Mn_{0.5}PO₄F make it a promising candidate as cathode material for Sodium-ion batteries. In-situ XANES and XRD are therefore used to explore the sodium extraction/intercalation mechanism of Na₂Fe_{0.5}Mn_{0.5}PO₄F.

Fig. 4 shows the first charge profiles of Na₂Fe_{0.5}Mn_{0.5}PO₄F during in situ XANES measurements using different current density (i.e., 8 and 100 mA/g). The sodium composition, *x* in Na_{2-x}Fe_{0.5}Mn_{0.5}PO₄F, was calculated from the charge and mass of the active material, by assuming that all the current pass was due to sodium extraction. Two voltage plateaus at around 2.9 and 3.8 V marked as (I) and (II) are clearly observed in the charge profile.

Fig. 5 shows normalized Fe and Mn K-edge XANES spectra for the Na₂Fe_{0.5}Mn_{0.5}PO₄F electrode collected at different current density. When charging at a low current density (i.e., 8 mA/g, which is close to the quasi-equilibrium state), the Fe K-edge shifts substantially to

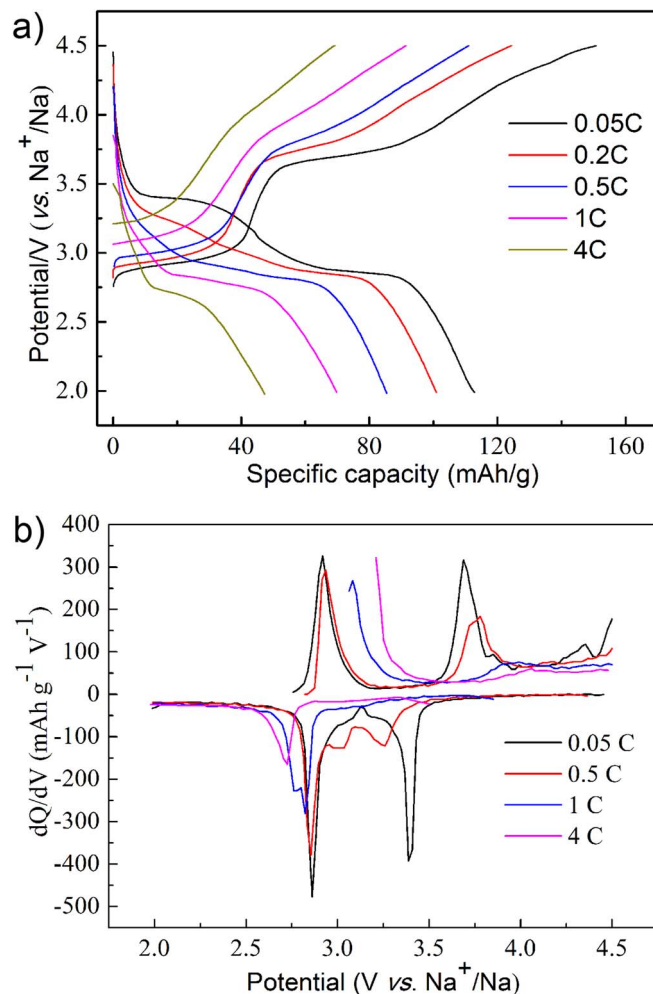


Figure 3. The first charge/discharge profiles (a) and dQ/dV curves (b) of Na₂Fe_{0.5}Mn_{0.5}PO₄F/Na cells at various rates.

higher energy values during the first charging plateau until $x \sim 0.47$ (region I). However, no significant change is observed for the Mn K-edge spectra during the same period of charging up to $x \sim 0.47$. With further charging to $x \sim 1.0$ (region II), the Mn K-edge starts to shift to higher energy values, while the Fe K-edge XANES spectra is almost identical. Spectroscopic behavior of Fe and Mn K-edge XANES for Na₂Fe_{0.5}Mn_{0.5}PO₄F electrode in Figs. 5a and 5b is very similar to previous Fe and Mn K-edge XANES results on LiFe_{1-x}Mn_xPO₄.^{31,32} This indicates that charge compensation in the first half of the charging process at a potential plateau of ~ 2.9 V is achieved mainly via the oxidation of Fe²⁺ ions. In contrast, the charge compensation in the other half of the charging process at a potential plateau of ~ 3.8 V is achieved mainly via the oxidation of Mn²⁺ ions. When charging at a high current density (i.e., 100 mA/g), the Fe K-edge XANES show similar spectroscopic behavior with which observed at 8 mA/g. However, the Mn K-edge shift is smaller compared with which observed at 8 mA/g (Figs. 5b and 5d). The spectroscopic behavior of Fe and Mn K-edge XANES collected at different current density is consistent with the electrochemical performance of Na₂Fe_{0.5}Mn_{0.5}PO₄F electrode. At low current density, both the Fe²⁺/Fe³⁺ and Mn²⁺/Mn³⁺ redox couples show high electrochemical activity, as indicated by the high intensity of Fe²⁺/Fe³⁺ and Mn²⁺/Mn³⁺ redox peaks in dQ/dV curves and the large Fe and Mn K-edge shift. At high current density (100 mA/g), the Fe²⁺/Fe³⁺ redox couples can preserve its high electrochemical activity, the Fe K-edge shift to almost the same position as which observed at low current density (8 mA/g) (Figs. 5a and 5c). Nevertheless, the Mn K-

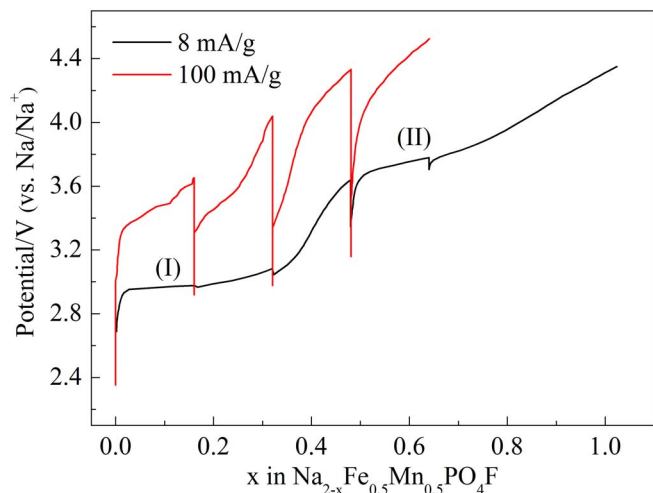


Figure 4. The first charge profiles of $\text{Na}_2\text{Fe}_{0.5}\text{Mn}_{0.5}\text{PO}_4\text{F}/\text{Na}$ cells for in situ XANES measurements using different current density.

edge shift at 100 mA/g is smaller compared with the shift observed at 8 mA/g. This indicates that the 3.8 V plateau corresponding to $\text{Mn}^{2+}/\text{Mn}^{3+}$ redox couple becomes indistinct with increasing current density, which can be attributed to the incompletely reaction of the $\text{Mn}^{3+}/\text{Mn}^{2+}$ redox couple. The rate capability of $\text{Na}_2\text{Fe}_{0.5}\text{Mn}_{0.5}\text{PO}_4\text{F}$ electrode is mainly restricted by the sluggish kinetic of $\text{Mn}^{2+}/\text{Mn}^{3+}$

redox couple. It has also been observed in $\text{LiMn}_x\text{Fe}_{1-x}\text{PO}_4$ system previously.^{29,30,33,34} This may be attributed to the lower electrical conductivity of Mn based polyanion materials compared with Fe based materials, and the poor reversibility of the $\text{Mn}^{2+}/\text{Mn}^{3+}$ redox couple compared with $\text{Fe}^{2+}/\text{Fe}^{3+}$ redox couple due to Jahn-Teller effect.

Fig. 6 shows in situ XRD results of $\text{Na}_2\text{Fe}_{0.5}\text{Mn}_{0.5}\text{PO}_4\text{F}$ electrode during the first cycle at 24.8 mA/g under constant current. It shows that the positions of Bragg peaks of $\text{Na}_2\text{Fe}_{0.5}\text{Mn}_{0.5}\text{PO}_4\text{F}$ electrode shift continuously throughout the charge-discharge process without emergence of new peaks, indicating a single phase solid solution Na^+ intercalation/extraction process. Careful inspection of the in-situ XANES data also reveals the absence of isosbestic points, suggesting the occurrence of a single phase topotactic reaction. This inference regarding the absence of a two-phase reaction is consistent with the in situ XRD results. The positions of the diffraction peaks shifted to high degree during the first oxidation and back to pristine position during the first reduction. This indicates the lattice parameters of $\text{Na}_2\text{Fe}_{0.5}\text{Mn}_{0.5}\text{PO}_4\text{F}$ decrease continuously with Na^+ extraction and increase reversibly with Na^+ intercalation. At the end of discharge, the diffraction peaks can fully return to the pristine position. This suggests that the sodiation/desodiation process in $\text{Na}_2\text{Fe}_{0.5}\text{Mn}_{0.5}\text{PO}_4\text{F}$ is reversible. Moreover, there are two important observations to be pointed out in the in situ XRD patterns. The first one is the continuous decrease in intensity and significant broadening of the diffraction peaks during the 3.8 V charge plateau corresponding to $\text{Mn}^{2+}/\text{Mn}^{3+}$ redox couple. At the end of charge, the sample displays a large decrease in crystallinity with some weak and broad peaks of $\text{Na}_{2-x}\text{Fe}_{0.5}\text{Mn}_{0.5}\text{PO}_4\text{F}$ recognizable in the XRD pattern. Such a decrease in crystallinity during desodiation process has also been reported in LiMnPO_4 during

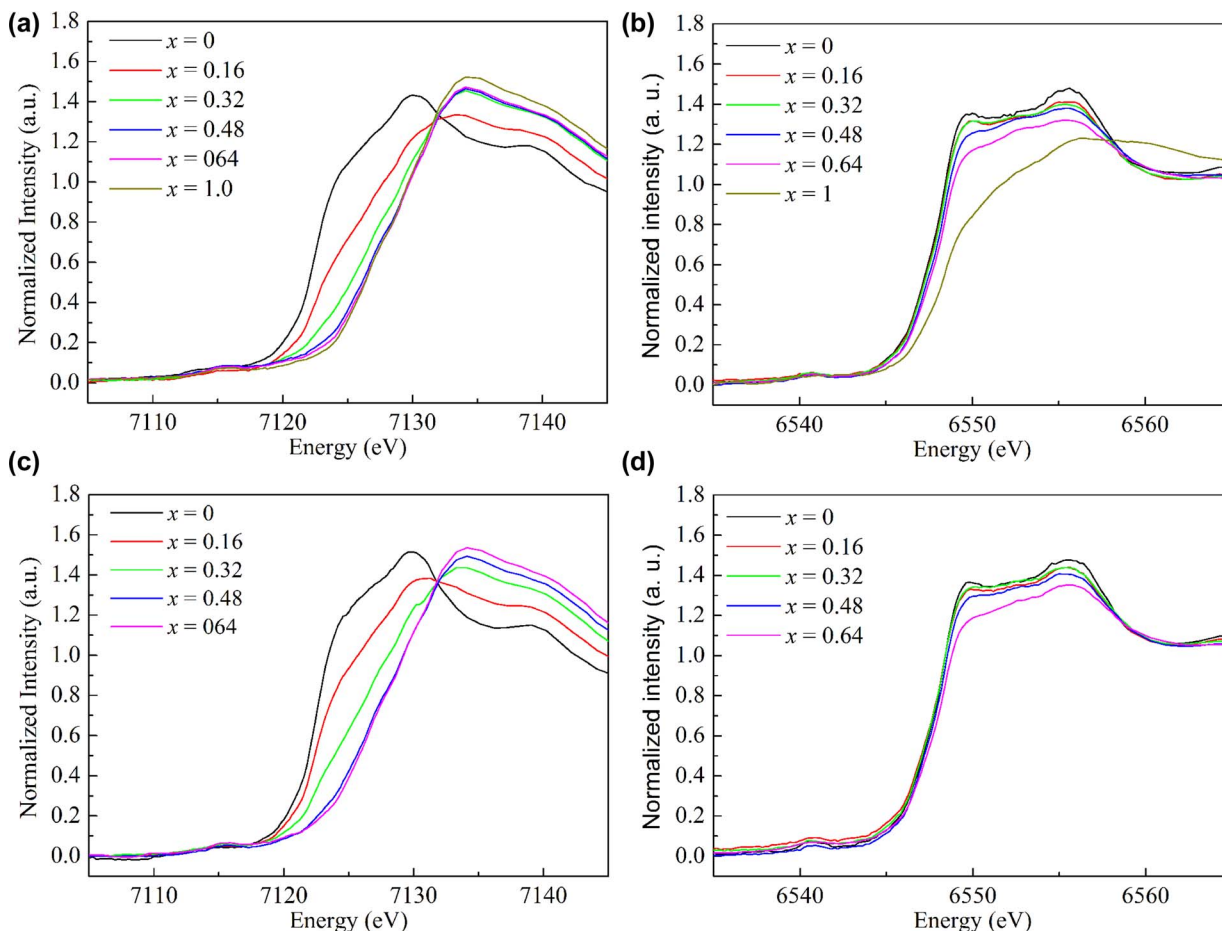


Figure 5. Normalized in situ Fe (a, c) and Mn (b, d) K-edge XANES spectra of $\text{Na}_2\text{Fe}_{0.5}\text{Mn}_{0.5}\text{PO}_4\text{F}$ collected at 8 (a, b) and 100 (c, d) mA/g during the first charge.

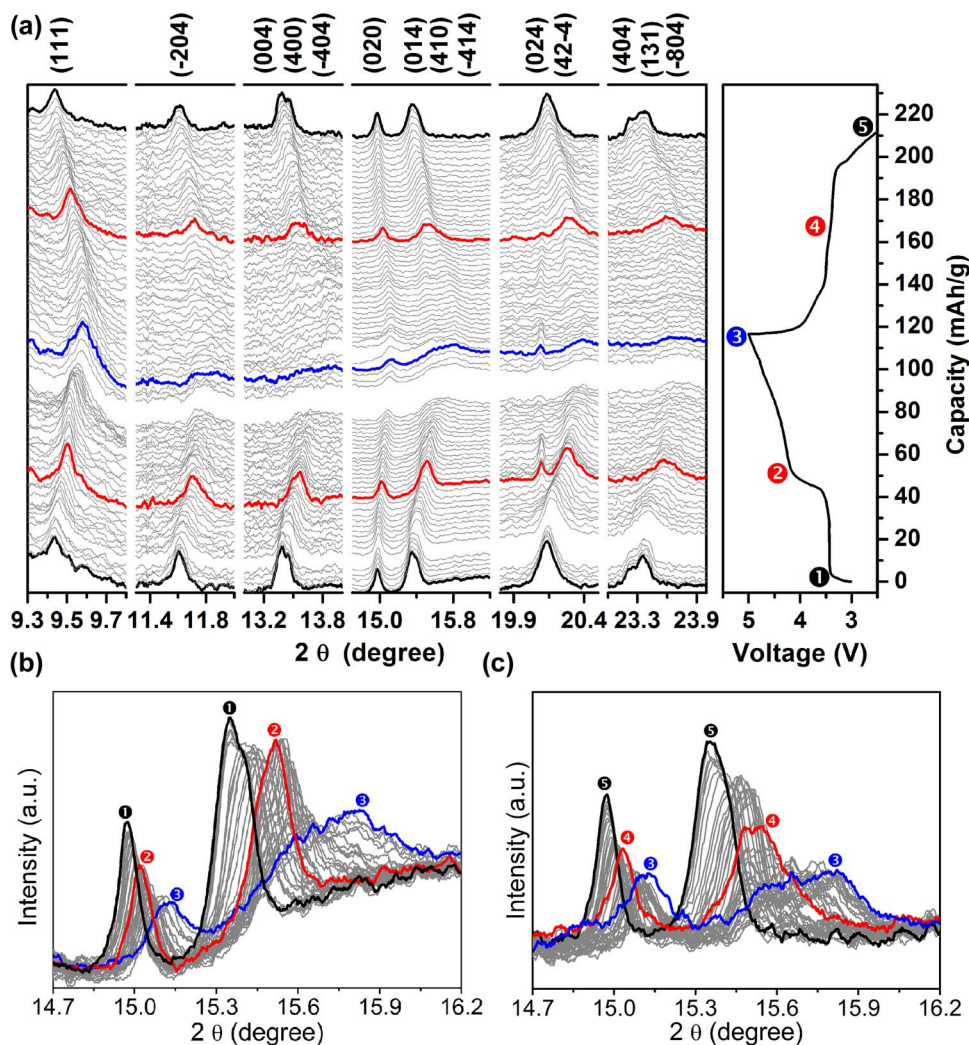


Figure 6. In situ XRD patterns of $\text{Na}_2\text{Fe}_{0.5}\text{Mn}_{0.5}\text{PO}_4\text{F}$ electrode during the first charge/discharge (a) and detailed view of 14.7° – 16.2° angular domains (b, c) ($\lambda = 0.6887 \text{ \AA}$).

chemical delithiation, which may be attributed to the elastic energy accumulated inside the lattice with an increase in the number of Jahn-Teller active Mn^{3+} ions.^{35,36} The second one is the diffraction peaks increase in intensity, and their positions and width revert to those of the initial $\text{Na}_2\text{Fe}_{0.5}\text{Mn}_{0.5}\text{PO}_4\text{F}$ at the end of discharge, indicating the good structural reversibility of $\text{Na}_2\text{Fe}_{0.5}\text{Mn}_{0.5}\text{PO}_4\text{F}$ during the electrochemical sodiation/desodiation. Unfortunately accurate determination of the lattice parameters evolution of $\text{Na}_2\text{Fe}_{0.5}\text{Mn}_{0.5}\text{PO}_4\text{F}$ electrode is made difficult by the decrease in intensity and significant broadening of the diffraction peaks during the 3.8 V charge plateau. Thus no further structural analysis could be done due to the low crystallinity of the electrode at the end of charging.

Recently, a similar structural change behavior in $\text{Na}_2\text{MnPO}_4\text{F}$ was reported by Lin et al. using ex situ XRD study, they showed a single phase reaction mode with obvious decreasing in crystallinity at the end of charging during electrochemical sodium extraction of $\text{Na}_2\text{MnPO}_4\text{F}$.¹⁶ Different with the single phase solid solution Na^+ intercalation/extraction behavior observed in $\text{Na}_2\text{Fe}_{0.5}\text{Mn}_{0.5}\text{PO}_4\text{F}$, a $\text{Na}_{1.5}\text{FePO}_4\text{F}$ intermediate phase with P2/c monoclinic structure between the two orthorhombic end-members $\text{Na}_2\text{FePO}_4\text{F}$ and NaFePO_4F was reported by Ellis et al. during the chemical oxidation of $\text{Na}_{2-x}\text{FePO}_4\text{F}$ in the sodium composition range of $0 \leq x \leq 1$.⁹ The slight monoclinic distortion of $\text{Na}_{1.5}\text{FePO}_4\text{F}$ appears to be driven by electron localization of $\text{Fe}^{2+}/\text{Fe}^{3+}$ in $\text{Na}_{1.5}\text{FePO}_4\text{F}$. The difference in structural change behavior between $\text{Na}_2\text{Fe}_{0.5}\text{Mn}_{0.5}\text{PO}_4\text{F}$

and $\text{Na}_2\text{FePO}_4\text{F}$ can be attributed to their difference in structure. The single phase reaction in $\text{Na}_2\text{Fe}_{0.5}\text{Mn}_{0.5}\text{PO}_4\text{F}$ can be beneficial to both of the charge movement and the subsequent phase boundary movement, thus enhance the electrochemical active of $\text{Na}_2\text{Fe}_{0.5}\text{Mn}_{0.5}\text{PO}_4\text{F}$ cathode.^{37,38} The good structural reversibility and single phase solid solution reaction mode indicate $\text{Na}_2\text{Fe}_{0.5}\text{Mn}_{0.5}\text{PO}_4\text{F}$ is a promising cathode material for sodium ion batteries.

Conclusions

Three-dimensional (3D) tunnel structure $\text{Na}_2\text{Fe}_{0.5}\text{Mn}_{0.5}\text{PO}_4\text{F}$ with high electrochemical performance was synthesized by a solid-state method. And the charge-discharge behaviors of $\text{Na}_2\text{Fe}_{0.5}\text{Mn}_{0.5}\text{PO}_4\text{F}$ were investigated by in situ Fe and Mn K-edge XANES and XRD techniques during the first cycle. The as prepared $\text{Na}_2\text{Fe}_{0.5}\text{Mn}_{0.5}\text{PO}_4\text{F}$ delivers a discharge capacity of 107 mAh/g at 12.4 mA/g with two well-defined voltage plateaus centered at 2.9 and 3.5 V vs. Na/Na^+ . In situ XANES results show that the major charge compensation at the metal site during desodiation at low current density (8 mA/g) is achieved by the oxidation of Fe^{2+} ions at lower potential plateau (~ 2.9 V) and the oxidation of Mn^{2+} ions at higher potential plateau (~ 3.8 V). Comparing the Fe and Mn K-edge XANES spectroscopic behaviors at different current density, it is concluded that the rate capability of $\text{Na}_2\text{Fe}_{0.5}\text{Mn}_{0.5}\text{PO}_4\text{F}$ electrode is mainly restricted by the sluggish kinetic of $\text{Mn}^{3+}/\text{Mn}^{2+}$ redox couple. This is consistent

with the electrochemical behaviors of $\text{Na}_2\text{Fe}_{0.5}\text{Mn}_{0.5}\text{PO}_4\text{F}$ at high rates. In situ XRD reveals a single phase solid solution Na^+ intercalation/extraction process and a reversible structural evolution process during the first cycle.

Acknowledgments

This work was supported by the National Key Research and Development Program (grant No. 2016YFB0901502), National Natural Science Foundation of China (grants Nos. 21303147, 21233004, 21473148) and Natural Science Foundation of Fujian Province of China (grant No. 2014J05019). The authors also thank beamlines BL14B1 and BL14W1 of SSRF (Shanghai Synchrotron Radiation Facility) for providing beam time.

References

1. V. Palomares, M. Casas-Cabanas, E. Castillo-Martinez, M. H. Han, and T. Rojo, *Energ. Environ. Sci.*, **6**, 2312 (2013).
2. N. Yabuuchi, K. Kubota, M. Dahbi, and S. Komaba, *Chem. Rev.*, **114**, 11636 (2014).
3. M. Sawicki and L. L. Shaw, *Rsc Adv.*, **5**, 53129 (2015).
4. D. Kundu, E. Talaie, V. Duffort, and L. F. Nazar, *Angew. Chem.-Int. Edit.*, **54**, 3431 (2015).
5. H. L. Pan, Y. S. Hu, and L. Q. Chen, *Energ. Environ. Sci.*, **6**, 2338 (2013).
6. Y. Kawabe, N. Yabuuchi, M. Kajiyama, N. Fukuhara, T. Inamasu, R. Okuyama, I. Nakai, and S. Komaba, *Electrochemistry*, **80**, 80 (2012).
7. Y. Kawabe, N. Yabuuchi, M. Kajiyama, N. Fukuhara, T. Inamasu, R. Okuyama, I. Nakai, and S. Komaba, *Electrochem. Commun.*, **13**, 1225 (2011).
8. I. K. Lee, I. B. Shim, and C. S. Kim, *J. Appl. Phys.*, **109**, 07E136 (2011).
9. B. L. Ellis, W. R. M. Makahnouk, W. N. Rowan-Weetaluktuk, D. H. Ryan, and L. F. Nazar, *Chem. Mater.*, **22**, 1059 (2010).
10. R. Tripathi, S. M. Wood, M. S. Islam, and L. F. Nazar, *Energ. Environ. Sci.*, **6**, 2257 (2013).
11. B. L. Ellis, W. R. M. Makahnouk, Y. Makimura, K. Toghill, and L. F. Nazar, *Nat. Mater.*, **6**, 749 (2007).
12. D. M. Cui, S. S. Chen, C. Han, C. C. Ai, and L. J. Yuan, *J. Power Sources*, **301**, 87 (2016).
13. N. Recham, J. N. Chotard, L. DuPont, K. Djellab, M. Armand, and J. M. Tarascon, *J. Electrochem. Soc.*, **156**, A993 (2009).
14. H. Zou, S. D. Li, X. B. Wu, M. J. McDonald, and Y. Yang, *ECS Electrochem. Lett.*, **4**, A53 (2015).
15. K. Kubota, K. Yokoh, N. Yabuuchi, and S. Komaba, *Electrochemistry*, **82**, 909 (2014).
16. X. C. Lin, X. Hou, X. B. Wu, S. H. Wang, M. Gao, and Y. Yang, *Rsc Adv.*, **4**, 40985 (2014).
17. Y. Zheng, P. Zhang, S. Q. Wu, Y. H. Wen, Z. Z. Zhu, and Y. Yang, *J. Electrochem. Soc.*, **160**, A927 (2013).
18. S. W. Kim, D. H. Seo, H. Kim, K. Y. Park, and K. Kang, *Phys. Chem. Chem. Phys.*, **14**, 3299 (2012).
19. X. B. Wu, J. M. Zheng, Z. L. Gong, and Y. Yang, *J. Mater. Chem.*, **21**, 18630 (2011).
20. J. H. Yan, X. B. Liu, and B. Y. Li, *Electrochem. Commun.*, **56**, 46 (2015).
21. M. Law, V. Ramar, and P. Balaya, *Rsc Adv.*, **5**, 50155 (2015).
22. T. Broux, T. Bamine, L. Simonelli, L. Stievano, F. Fauth, M. Ménétrier, D. Carlier, C. Masquelier, and L. Croguennec, *J. Phys. Chem. C*, **121**, 4103 (2017).
23. W. M. Dose, N. Sharma, J. C. Pramudita, J. A. Kimpton, E. Gonzalo, M. H. Han, and T. Rojo, *Chem. Mater.*, **28**, 6342 (2016).
24. N. Sharma, E. Gonzalo, J. C. Pramudita, M. H. Han, H. E. A. Brand, J. N. Hart, W. K. Pang, Z. Guo, and T. Rojo, *Adv. Funct. Mater.*, **25**, 4994 (2015).
25. V. Palomares, P. Serras, H. E. A. Brand, T. Rojo, and N. Sharma, *J. Mater. Chem. A*, **3**, 23017 (2015).
26. N. Sharma, P. Serras, V. Palomares, H. E. A. Brand, J. Alonso, P. Kubiak, M. L. Fdez-Gubieda, and T. Rojo, *Chem. Mater.*, **26**, 3391 (2014).
27. P. Serras, V. Palomares, J. Alonso, N. Sharma, J. M. L. del Amo, P. Kubiak, M. L. Fdez-Gubieda, and T. Rojo, *Chem. Mater.*, **25**, 4917 (2013).
28. A. von Cresce and K. Xu, *J. Electrochem. Soc.*, **158**, A337 (2011).
29. M. Yonemura, A. Yamada, Y. Takei, N. Sonoyama, and R. Kanno, *J. Electrochem. Soc.*, **151**, A1352 (2004).
30. C. Delacourt, L. Laffont, R. Bouchet, C. Wurm, J. B. Leriche, M. Morcrette, J. M. Tarascon, and C. Masquelier, *J. Electrochem. Soc.*, **152**, A913 (2005).
31. K. W. Nam, W. S. Yoon, K. Zaghbi, K. Y. Chung, and X. Q. Yang, *Electrochem. Commun.*, **11**, 2023 (2009).
32. A. Yamada, Y. Kudo, and K. Y. Liu, *J. Electrochem. Soc.*, **148**, A747 (2001).
33. C. Delacourt, P. Poizot, M. Morcrette, J. M. Tarascon, and C. Masquelier, *Chem. Mater.*, **16**, 93 (2004).
34. K. Saravanan, V. Ramar, P. Balaya, and J. J. Vittal, *J. Mater. Chem.*, **21**, 14925 (2011).
35. A. Yamada, Y. Takei, H. Koizumi, N. Sonoyama, R. Kanno, K. Itoh, M. Yonemura, and T. Kamiyama, *Chem. Mater.*, **18**, 804 (2006).
36. Y. Q. Huang, N. A. Chernova, Q. Y. Yin, Q. Wang, N. F. Quackenbush, M. Leskes, J. Fang, F. Omenya, R. B. Zhang, M. J. Wahila, L. F. J. Piper, G. W. Zhou, C. P. Grey, and M. S. Whittingham, *Inorg. Chem.*, **55**, 4335 (2016).
37. G. Kobayashi, S. I. Nishimura, M. S. Park, R. Kanno, M. Yashima, T. Ida, and A. Yamada, *Adv. Funct. Mater.*, **19**, 395 (2009).
38. N. Meethong, H. Y. S. Huang, W. C. Carter, and Y. M. Chiang, *Electrochem. Solid State Lett.*, **10**, A134 (2007).